SOLAR CELLS

Monolithic perovskite/silicon tandem solar cell with >29% efficiency by enhanced hole extraction

Amran Al-Ashouri[1]*, Eike Köhnen[1]*, Bor Li[1], Artiom Magomedov[2], Hannes Hempel[3], Pietro Caprioglio[1,4], José A. Márquez[3], Anna Belen Morales Vilches[5], Ernestas Kasparavicius[2], Joel A. Smith[6,7], Nga Phung[6], Dorothee Menzel[1], Max Grischek[1,4], Lukas Kegelmann[1], Dieter Skroblin[8], Christian Gollwitzer[8], Tadas Malinauskas[2], Marko Jošt[1,9], Gašper Matič[9], Bernd Rech[10,11], Rutger Schlatmann[5,12], Marko Topič[9], Lars Korte[1], Antonio Abate[6], Bernd Stannowski[5,13], Dieter Neher[4], Martin Stolterfoht[4], Thomas Unold[3], Vytautas Getautis[2], Steve Albrecht[1,11]†

Tandem solar cells that pair silicon with a metal halide perovskite are a promising option for surpassing the single-cell efficiency limit. We report a monolithic perovskite/silicon tandem with a certified power conversion efficiency of 29.15%. The perovskite absorber, with a bandgap of 1.68 electron volts, remained phase-stable under illumination through a combination of fast hole extraction and minimized nonradiative recombination at the hole-selective interface. These features were made possible by a self-assembled, methyl-substituted carbazole monolayer as the hole-selective layer in the perovskite cell. The accelerated hole extraction was linked to a low ideality factor of 1.26 and single-junction fill factors of up to 84%, while enabling a tandem open-circuit voltage of as high as 1.92 volts. In air, without encapsulation, a tandem retained 95% of its initial efficiency after 300 hours of operation.

A tandem solar cell, consisting of a silicon cell overlaid by a perovskite solar cell (PSC) (*1*), could increase efficiencies of commercial mass-produced photovoltaics beyond the single-junction cell limit (*1*, *2*) without adding substantial cost (*3*, *4*). The certified power conversion efficiency (PCE) of PSCs has reached up to 25.5% for single-junction solar cells (usual active area of ~0.1 cm^2) (*5*), 24.2% for perovskite/CIGSe (copper-indium-gallium-selenide) tandem cells (~1 cm^2) (*5*–*7*), 24.8% for all-perovskite tandem cells (0.05 cm^2) (*8*, *9*), and 26.2% for the highest openly published perovskite/silicon tandem efficiency (~1 cm^2) (*10*). Perovskite/silicon tandem cells have additionally undergone technological advances in both stability and compatibility with textured silicon substrates (*11*–*13*). However, these perovskite-based tandem solar cells still have room for improvement, as practical limits for all these tandem technologies are well above 30% (*14*, *15*).

The increase in PSC efficiency has been driven in part by advances in physical and chemical understanding of the defect and recombination mechanisms. Some reports presented near-perfect passivation of surfaces and grain boundaries, with photoluminescence quantum yields (PLQYs) approaching theoretical limits (*16*–*18*). Consequently, PSCs were reported with open-circuit voltage (V_{OC}) values of only a few tens of meV below their radiative limit (*19*–*23*). These values surpass those reached with crystalline silicon absorbers and are comparable with solar cells based on epitaxially grown GaAs (*23*, *24*). However, perovskite compositions with a wider bandgap that are needed for high-efficiency tandem solar cells still show considerable V_{OC} losses (*14*, *25*). The main reasons include comparably low PLQYs of the absorber material itself, an unsuitable choice of selective contacts, and phase instabilities. Even state-of-the-art perovskite/silicon tandem cells still have V_{OC} values well below 1.9 V.

We present a strategy to overcome these issues simultaneously, demonstrated with a triple-cation perovskite composition with a bandgap of 1.68 eV, which enables photostable tandem devices with a V_{OC} of 1.92 V. We note that the charge extraction efficiency, and hence the fill factor (FF), of PSCs is still poorly understood. Although reported PSCs usually feature a small active area (~0.1 cm^2) with small absolute photocurrents (a few milliamperes), and thus small series resistance losses at the contacts, typical FFs of high-efficiency devices generally range from 79 to 82%. However, on the basis of the detailed balance limit, PSCs should be able to deliver a FF of 90.6% at a bandgap of 1.6 eV. Wider-bandgap perovskite compositions near 1.7 eV seem especially prone to low FFs, resulting in tandem cell FF values commonly below 77%, near current-matching conditions (*11*, *12*, *26*). In optimized perovskite single-junction devices, the FFs only recently exceeded 80%, with a maximum value of 84.8% (*27*).

One reason for the low FF might be that there are only a few techniques for quantifying and analyzing the FF losses in PSCs. We show that intensity-dependent transient photoluminescence in combination with absolute photoluminescence is a viable technique for doing so. A main FF limitation of high-efficiency PSCs is the ideality factor n_{ID}, with typical values of 1.4 to 1.8 for high-V_{OC} devices (*28*), whereas established solar cell technologies reach values of 1 to 1.3 (*29*). Thus, an important goal for perovskite photovoltaics is to lower the ideality factor while minimizing nonradiative interface recombination to achieve a high V_{OC} (*28*). We designed a self-assembled monolayer (SAM) with methyl group substitution as a hole-selective layer, named Me-4PACz ([4-(3,6-dimethyl-9H-carbazol-9-yl)butyl]phosphonic acid) and show that a fast hole extraction went along with a lower ideality factor. Thus, FFs of up to 84% in p-i-n single-junction PSCs and >80% in tandem devices were achieved.

The SAM provided both fast extraction and efficient passivation at the hole-selective interface. This combination slowed light-induced halide segregation of a tandem-relevant perovskite composition with 1.68-eV bandgap, allowed a PLQY as high as on quartz glass, and led to high single-junction device V_{OC} values of >1.23 V. The single-junction improvements transferred into tandem devices, which allowed us to fabricate perovskite/silicon tandem solar cells with a certified PCE of 29.15%. This value surpasses the best silicon single-junction cell (26.7%) and is comparable to the best GaAs solar cell (*27*) at the same area of 1 cm^2. Under maximum power point (MPP) tracking in ambient air without encapsulation, a Me-4PACz tandem cell retained 95% of its initial efficiency after 300 hours. We used injection-dependent absolute electroluminescence (EL) spectroscopy to reconstruct the individual subcell current-voltage curves without the influence of series resistance (pseudo–*J-V* curves), which showed that the tandem device design that features only a standard perovskite film without additional bulk passivation could in principle realize PCE values up to 32.4%.

Stabilization of wide-bandgap perovskite with the hole-selective layer

The ideal top cell bandgap for perovskite absorbers in conjunction with CIGSe and Si bottom cells is ~1.68 eV (*30*–*32*). These wider-bandgap compositions often feature a Br/I ratio of >20%, which can lead to phase instabilities caused by light-induced halide segregation, most strikingly evident from photoluminescence (PL)

---

[1]Young Investigator Group Perovskite Tandem Solar Cells, Helmholtz-Zentrum Berlin, 12489 Berlin, Germany. [2]Department of Organic Chemistry, Kaunas University of Technology, Kaunas LT-50254, Lithuania. [3]Department of Structure and Dynamics of Energy Materials, Helmholtz-Zentrum Berlin für Materialien und Energie GmbH, 14109 Berlin, Germany. [4]Institute of Physics and Astronomy, University of Potsdam, 14476 Potsdam, Germany. [5]PVcomB, Helmholtz-Zentrum Berlin, 12489 Berlin, Germany. [6]Young Investigator Group Active Materials and Interfaces for Stable Perovskite Solar Cells, Helmholtz-Zentrum Berlin, 12489 Berlin, Germany. [7]Department of Physics and Astronomy, University of Sheffield, Sheffield S3 7RH, UK. [8]Physikalisch-Technische Bundesanstalt, 10587 Berlin, Germany. [9]Faculty of Electrical Engineering, University of Ljubljana, 1000 Ljubljana, Slovenia. [10]Scientific Management, Helmholtz-Zentrum Berlin, 12489 Berlin, Germany. [11]Faculty of Electrical Engineering and Computer Science, Technical University Berlin, 10587 Berlin, Germany. [12]HTW Berlin–University of Applied Sciences, 12459 Berlin, Germany. [13]Beuth University of Applied Sciences Berlin, 13353 Berlin, Germany.
*These authors contributed equally to this work.
†Corresponding author. Email: steve.albrecht@helmholtz-berlin.de

spectra that show a double-peak formation under continuous illumination (*33*, *34*). Upon generation of charge carriers in the perovskite film, iodide-rich clusters can form that are highly luminescent because they serve as charge carrier sinks, given their lower bandgap relative to the surrounding material (*35*). As quantified by Mahesh *et al.*, although some portion of the V_{OC} loss is related to halide segregation, the dominant source of V_{OC} loss is likely the generally low optoelectronic quality of the Br-rich mixed-halide perovskite absorbers, or high nonradiative recombination rates at their interfaces (*35*). Hence, to unambiguously determine the limitations and potentials of wide-bandgap compositions, it is necessary to find suitable charge-selective contacts that do not introduce further losses or instabilities.

We show that fast charge extraction paired with surface passivation can effectively suppress the formation of a double-peak emission in the PL, indicative of phase stabilization, and simultaneously enable a high quasi–Fermi level splitting (QFLS) and device performance. Rather than optimizing the perovskite composition or passivating the film, we chose a variant of the widely used Cs-, FA-, and MA-containing "triple-cation" perovskite (*36*) that is highly reproducible (FA, formamidinium; MA, methylammonium) and focused on preparing an optimal charge-selective contact on which the perovskite film was deposited. We enlarged the bandgap by increasing the Br/I ratio to obtain a 1.68-eV (23% Br) absorber instead of the commonly used 1.60 to 1.63 eV (~17% Br), yielding a nominal precursor composition of $Cs_{0.05}(FA_{0.77}MA_{0.23})_{0.95}Pb(I_{0.77}Br_{0.23})_3$.

A schematic of the device stack and the hole-selective layers (commonly abbreviated as HTLs, "hole-transporting layers") used for PL measurements is shown in Fig. 1. We first compared the QFLS measured by absolute PL and then the PL stability of this perovskite composition prepared on indium tin oxide (ITO) substrates covered by the HTLs. In recently published high-PCE p-i-n ("inverted") single-junction and tandem PSCs, the polymer poly[bis(4-phenyl)(2,4,6-trimethylphenyl)amine] (PTAA) or the comparable poly[*N*,*N*′-bis(4-butylphenyl)-*N*,*N*′-bis(phenyl)-benzidine] (polyTPD) is typically used (*10*, *11*, *37*, *38*). Alternatively, SAMs based on carbazole, such as MeO-2PACz and 2PACz, can form passivated interfaces while allowing for low transport losses because they are ultrathin (<1 nm) (*7*). The introduction of a methyl-group substitution to the "lossless" hole-selective interface created by 2PACz (*7*) led to a more optimized alignment with the perovskite valence band edge (see energetic band edge diagram in fig. S1) with a similar dipole moment (~1.7 D) and resulted in faster charge extraction. The supplementary materials contain the synthesis scheme of the SAMs we used. In the literature concerning the n-i-p configuration of PSCs, methoxy substituents are prevalent in HTLs, with some reports of a possible passivation function at the perovskite interface (*39*–*42*). For the p-i-n configuration, however, the standard high-performance HTLs PTAA and polyTPD contain alkyl substituents. In the present study, we directly compared methoxy and methyl substituents in p-i-n cells with MeO-2PACz and Me-4PACz, with the results showing advantages for the methyl substitution with respect to both passivation and hole extraction. We tested the influence of the aliphatic chain length (*n*) in carbazole-based SAMs without (nPACz) and with methyl substitution (Me-nPACz) on PSC performance and found an optimum FF at $n = 2$ for nPACz and $n = 4$ for Me-nPACz (see fig. S23). For $n = 6$, both SAMs led to current-voltage hysteresis.

The QFLS values of bare perovskite films (Fig. 1B) deposited on 2PACz and Me-4PACz were similar to that on quartz glass, commonly regarded as a perfectly passivated substrate (*16*). Perovskite compositions with high Br content typically segregate into I-rich phases indicated by increased PL intensity at lower photon energies, here at a wavelength of 780 nm (*33*). Pristine regions of the nonsegregated perovskite film emitted photons at a peak wavelength of ~740 nm for perovskite deposited on glass (Fig. 1C) or ITO/PTAA (Fig. 1D), and a similar response was seen for the SAM MeO-2PACz (fig. S3) on ITO. However, the perovskite emission was more stable over time on ITO/2PACz and ITO/Me-4PACz substrates (Fig. 1E and fig. S3). The raw spectra are shown in fig. S4.

Among the studied HTLs, phase segregation was inhibited only if the perovskite was grown on a substrate that fulfilled the requirements of both fast charge extraction and good passivation; Fig. 1F shows that passivation alone was insufficient. The black curve shows a PL spectrum of the perovskite film on an insulating glass substrate that was covered by Me-4PACz after 10 min of continuous spot illumination with 1-sun equivalent photon flux. The illuminated film showed signs of I-rich phases emitting at a center wavelength of ~780 nm. The glass substrate ensured that no hole transfer out of the perovskite bulk occurred. In contrast, a conductive ITO substrate that allowed hole transmission in combination with Me-4PACz increased the PL stability, as evidenced by the sharp peak with emission centered at ~740 nm even after 10 min of spot illumination.

A bare ITO substrate seemed to prevent charge accumulation as well, allowing a stable PL peak position at 1-sun intensity (spot size 0.12 cm^2; see fig. S6). The connection between charge accumulation in the perovskite and phase instability was reported in previous studies in which a reduced density of carriers increased the activation energy of mobile ion species and allowed the film to remain in its initial form (*43*, *44*). Spot illumination (0.12 cm^2 with 1-sun photon flux) represented increased stress testing on phase stability compared to full illumination because it created an outward driving force for ions from the illuminated area (*45*). Consequently, a smaller illumination spot (i.e., larger edge-to-area ratio) at the same illumination intensity showed a faster PL redshift (see figs. S5 and S6). To compare the degree of PL redshift and double-peak formation, we evaluated the ratio of the two emission center intensities at 740 and 780 nm for two different excitation fluences equivalent to 1-sun and 30-sun illumination (Fig. 1, G and H). At 1-sun–equivalent intensity, only 2PACz and Me-4PACz on ITO had a stable ratio. However, upon increasing the intensity and thus the charge carrier generation rate by a factor of 30, a Me-4PACz–covered ITO substrate differed from the 2PACz–covered substrate by still displaying a similarly stable PL intensity ratio.

We used transient photoluminescence (TrPL) to analyze charge carrier transfer into adjacent charge-selective layers (*46*). The full decay is governed by nonradiative, trap-assisted surface/bulk recombination (mostly monoexponential decay), radiative recombination ("bimolecular," second-order decay), and charge transfer effects, which can be disentangled if these time constants differ sufficiently from each other (*18*). Figure 2A presents PL transients of 1.68 eV–bandgap perovskite films on ITO/HTL substrates. With MeO-2PACz and PTAA, it was not possible to clearly differentiate between charge extraction and trap-assisted recombination because the nonradiative recombination was high (as evidenced by lower QFLS values relative to quartz glass; Fig. 1B) and because the transients did not saturate toward one process. In contrast, the PL transients for 2PACz and Me-4PACz showed a clear monoexponential decay at later times, indicating Shockley-Read-Hall recombination (*47*). Fits to the TrPL transients (fig. S8) were used to compute the differential lifetime $\tau = -\{d \ln[\phi(t)]/dt\}^{-1}$ (Fig. 2B), where $\phi(t)$ is the time-dependent PL photon flux. In this representation, the processes that reduce the PL counts over time are separable, and the transient decay time (or "lifetime") is directly readable at each time point (*46*).

The asymptotically reached high TrPL lifetimes of >5 μs for both 2PACz and Me-4PACz suggests that there were minimal nonradiative recombination losses at the SAM interfaces. The charge transfer process at early times (until ~1 μs) led to a sharp rise of τ, resembling simulated curves by Krogmeier *et al.* (*46*). The transition from increasing lifetime to the plateau marks the end of charge transfer, and nonradiative first-order recombination becomes dominant. Because PLQY measurements of films on 2PACz and Me-4PACz indicated a similar level of interface recombination under the same charge generation conditions (see also fig. S9), the steepness of this rise was influenced by the charge transfer speed. The observed gradient for Me-4PACz implied a faster hole transfer to the underlying ITO relative to 2PACz, with the saturation starting after ~300 ns rather than ~1 µs.

In the charge carrier generation regime of this experiment (~1 sun, ~3 × 10^{15} cm^{-3}), trap-assisted recombination dominated, with the PL flux scaling proportionally to the density of photogenerated carriers n, as evidenced by intensity-dependent TrPL shown in fig. S9. Figure S9 further demonstrates that at higher generation conditions, the PL flux scaled proportionally to n^2, where transients usually show a multiexponential signature, as seen with 2PACz and quartz (fig. S10). Nonetheless, in this regime the Me-4PACz transients remained monoexponential until generation densities exceeded ~35 suns equivalent. We interpret this as a consequence of a large hole-extraction flux, which causes first-order recombination to dominate even in this injection regime.

We quantify this phenomenon of persisting domination of first-order recombination in Fig. 2C by displaying the ratio of higher-order

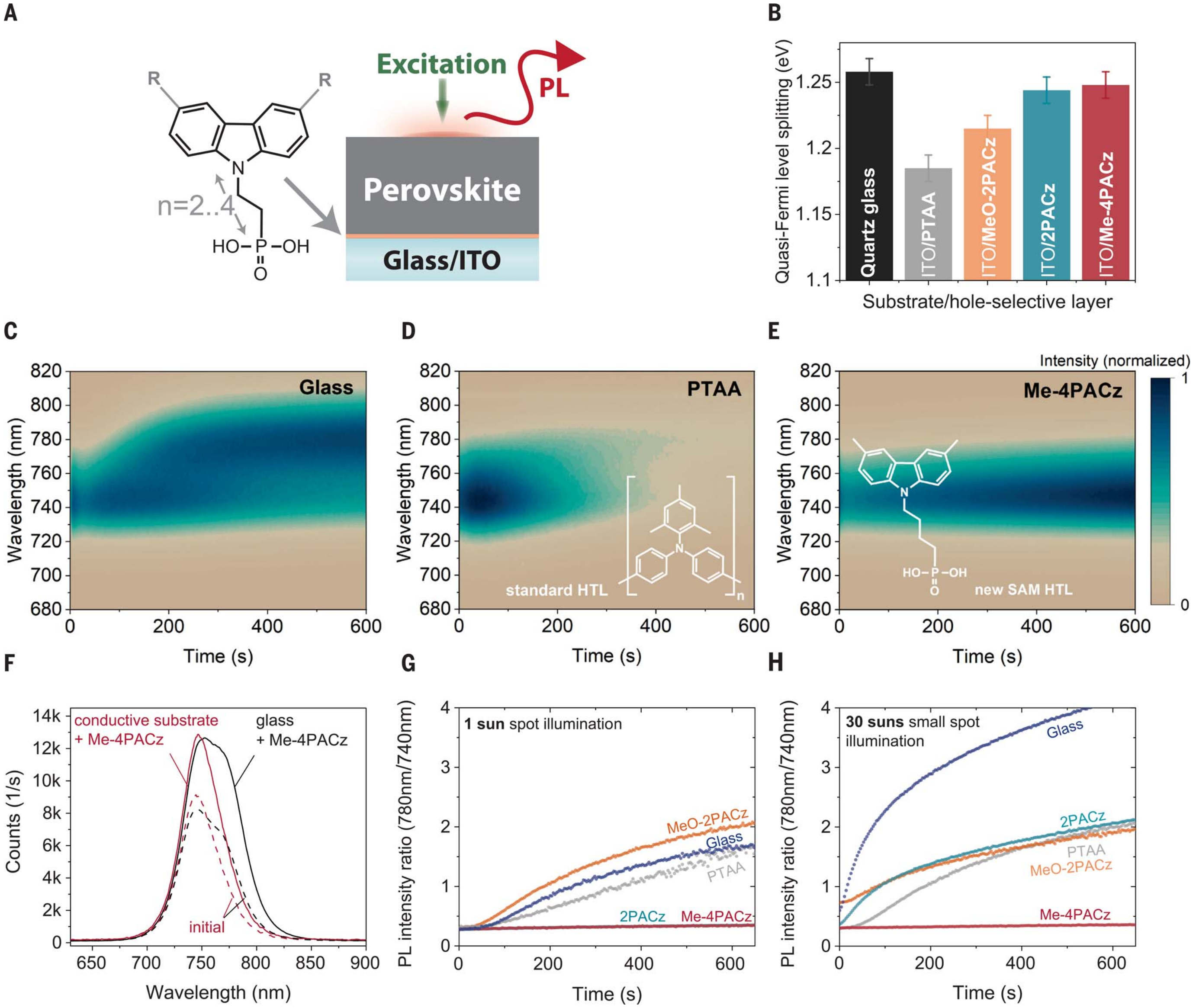

Fig. 1. Photoluminescence properties and stability assessment of perovskite films on different substrates. (**A**) Schematic description of the photoluminescence (PL) experiment and chemical structure of a general carbazole-based SAM, with R denoting a substitution, which in this work is either nothing (2PACz), a methoxy group (MeO-2PACz), or a methyl group (Me-4PACz). The number 2 or 4 denotes the number of the linear C atoms between the phosphonic acid anchor group and the conjugated carbazole main fragment. (**B**) Quasi–Fermi level splitting (QFLS) values of nonsegregated 1.68-eV bandgap perovskite films on a bare glass substrate and different hole-selective layers on the transparent and conductive indium tin oxide (ITO). Error bars denote the global error of the evaluation method (~20 meV). (**C** to **E**) Time-dependent photoluminescence spectra analyzing phase stability of perovskite absorbers with 1.68-eV bandgap. The perovskite films were deposited either on glass (C) or on ITO substrates with different hole-selective layers [(D) and (E)]. The color scale is at the far right. (**F**) PL spectra before (dashed lines) and after 600 s of light-soaking (solid lines) under 1-sun equivalent illumination in air, comparing the perovskite grown on Me-4PACz that had been deposited on a glass substrate and a conductive ITO substrate. (**G**) Ratio of PL intensities at 780 nm (I-rich domains) and 740 nm (neat perovskite) from the PL evolutions in (C), (D), (E), and two other hole-selective layers (see fig. S4; illumination spot size ~0.12 cm^2), shown as a figure of merit for phase stability. (**H**) Ratio of PL intensities as in (G), but at higher illumination intensity through decrease of the excitation spot size to 0.4 mm^2.

to first-order recombination for the different generation conditions (see supplementary text for the evaluation method). Comparison of Me-4PACz to 2PACz indicates that the hole-extraction flux of Me-4PACz was larger by a factor of >10, because the curvature of the TrPL transient only begins to resemble that of 2PACz at a factor of >10 higher generation density (indicated by the blue dashed line in Fig. 2C).

The carrier mobilities determined by optical pump terahertz probe measurements (fig. S12) were similar between perovskite films grown on the different HTLs. To also exclude differences in perovskite composition and crystal orientation due to possible growth differences, we probed the effect of the HTL on these properties by grazing-incidence wide-angle x-ray scattering at the four-crystal monochromator beamline of the Physikalisch-Technische Bundesanstalt (*48*). Azimuthally integrated diffraction patterns collected on a movable PILATUS detector module (*49*) showed comparable composition in each case (fig. S13), with marginally increased PbI_2 scattering intensity on PTAA as we observed in our previous work (*7*). Comparing azimuthal intensity profiles for perovskite scattering features (fig. S14), we found a negligible difference in crystallographic orientation between the samples.

Our complete solar cells were capped by C_{60} as the electron-selective contact. The electron extraction speed did not limit the cell operation, as demonstrated by a time-resolved terahertz photoconductivity measurement combined with TrPL on a quartz/perovskite/C_{60} sample (fig. S11). We compared the decays of free charge carriers after interface-near carrier generation on both sample sides and found an electron transfer time constant of ~1 ns, substantially faster than hole transfer at the hole-selective layer (in the range of ~100 ns). The extraction velocity into the C_{60} in our model was 1.6×10^4 cm/s (see fig. S11 for details), a value similar to earlier reported velocities (*46*).

Performance of perovskite single-junction solar cells

For analysis at the solar cell level, we focused on the simple single-junction device stack glass/ITO/HTL/perovskite/C_{60}/SnO_2/Ag, with the SnO_2 serving as a buffer layer for indium zinc oxide (IZO) sputtering in the fabrication of tandem solar cells (*50*). We found that the combination of fast charge extraction and passivated interface not only mitigated phase instability (see Fig. 1) but was also linked to an increased FF of solar cell devices, mainly by a decreased diode ideality factor of the PSCs. The FF is the major remaining parameter for which PSCs have not yet come close to the values of established solar cell technologies (*24*, *51*) (see fig. S16 for FF comparisons), with the ideality factor being one of the main properties that limit high-efficiency PSCs (*29*). MeO-2PACz and 2PACz led to FFs of up to 82% (Fig. 3A), whereas with Me-4PACz the values were as high as 84%, representing ~93% of the radiative limit.

Figure 3B shows *J-V* curves recorded at simulated AM1.5G illumination conditions, comparing champion PTAA and Me-4PACz cells of the same batch and showing the superior performance of the SAM. The ideality factors n_{ID} for PSCs with different HTLs (Fig. 3C and Table 1) were ~1.26 for Me-4PACz, ~1.42 for 2PACz, 1.51 for MeO-2PACz, and ~1.55 for PTAA cells. Figure S20 compares the V_{OC} values achieved with the different HTLs. Despite the large differences in passivation at the hole-selective interface, the differences in V_{OC} were not as large (average difference of 30 mV between PTAA and Me-4PACz) because of the limiting nonradiative recombination at the C_{60} interface. However, as reasoned above, the C_{60} layer did not limit charge extraction, hence the different extraction speeds invoked by the HTLs directly influenced the FF values. The high FF with Me-4PACz was accompanied by high V_{OC} values of up to 1.16 V; when a LiF interlayer was placed between the perovskite and C_{60}, we achieved a maximum voltage of 1.234 V (*52*, *53*) (Fig. 3D and fig. S20). The combination of a high V_{OC} with low n_{ID} was previously considered as challenging for PSCs (*28*), and it allowed us to fabricate a perovskite single junction with a PCE of 20.8% with Me-4PACz (fig. S18) and a perovskite bandgap of 1.68 eV.

To investigate the FF values without the influence of series resistance losses, we measured intensity-dependent absolute PL spectra and computed the QFLS values [or implied V_{OC} (iV_{OC})] as a function of the illumination intensity. The derived data pairs of generation currents and iV_{OC} values allowed the reconstruction of hypothetical, so-called pseudo–*J-V* curves, as recently shown in (*54*) (Fig. 3D). The extracted FF and pseudo-FF values (FF in absence of transport losses) of bare perovskite films grown on different HTLs are summarized in Table 1, row 1. Both 2PACz and Me-4PACz enabled high "pseudo-FF" (pFF) values of ~88%, which is 96.8% of the detailed balance limit and similar to the value achieved on a bare quartz substrate. PTAA allowed for a pFF of only 85.6%.

This analysis highlights how the SAMs formed a practically lossless interface between ITO and perovskite. Interestingly, when including a C_{60} layer on top of the perovskite film, no

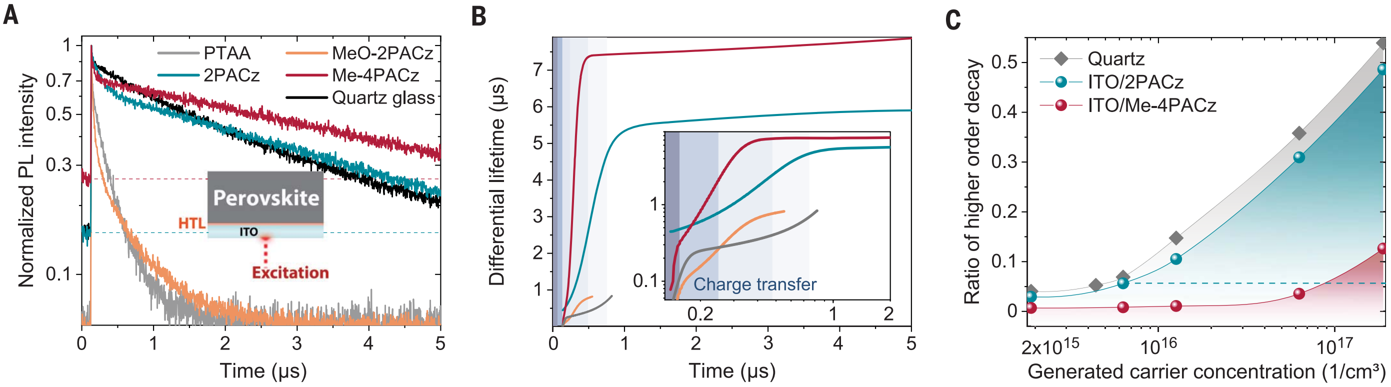

Fig. 2. Role of charge transfer in transient photoluminescence (TrPL). (**A**) PL transients of perovskite on ITO/hole-selective layer substrates. The dashed lines indicate the background levels. (**B**) Computed differential lifetimes from fits to the transients in (A), showing the single-exponential decay time at each time of the transient, with early times shown in the inset. The inset highlights the region of the Me-4PACz and 2PACz transients that is governed by hole transfer into the ITO. Excitation density is similar to 1-sun conditions (fluence of ~30 nJ/cm^2, 2×10^{15} to 3×10^{15} cm^{-3}). Colors are as in (A). The shaded areas are a guide marking the approximate time domain in which the Me-4PACz transient is governed by charge transfer. (**C**) Ratio of higher-order processes to monoexponential decay in the TrPL transients, revealing that Me-4PACz not only extracts holes faster [inset in (B)] but does so at ~10 times the efficiency of 2PACz, because the Me-4PACz transient shows the same magnitude of radiative recombination only with charge carrier generation that is higher by a factor of ~10 (comparison along the dashed line; see fig. S10 for details).

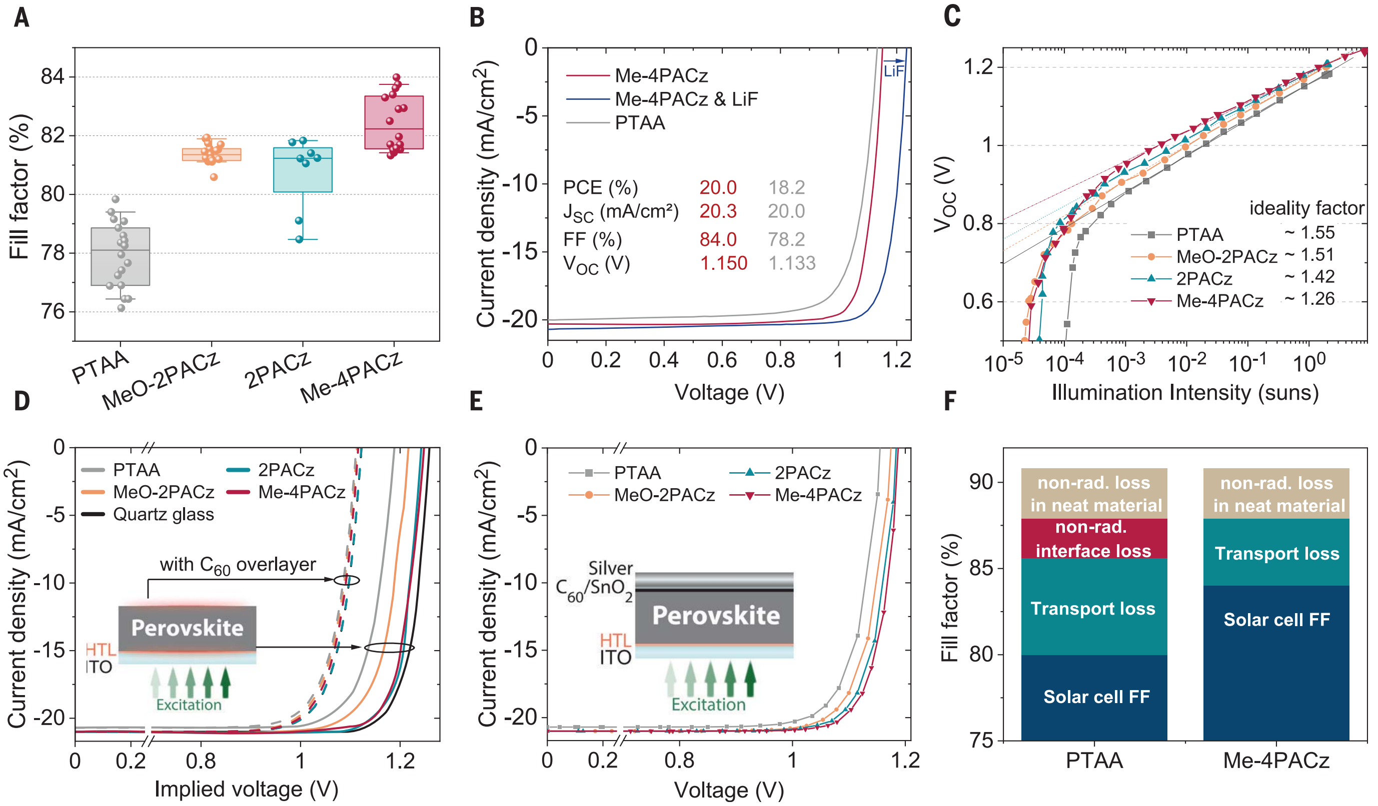

Fig. 3. Performance and fill factor loss analysis of p-i-n solar cells with different hole-selective layers. (**A**) Comparison of fill factor values of PSCs with the stack glass/ITO/HTL/perovskite/C_{60}/SnO_2/Ag, triple-cation perovskite absorber with 1.68-eV bandgap. All data are from cells made from the same perovskite precursor and contact processing batch. The boxes indicate the 25/75 percentiles; the whiskers indicate the 10/90 percentiles. (**B**) *J-V* curves of the best cells of the batch in (A) and a *J-V* curve of a Me-4PACz cell from another batch with LiF interlayer between C_{60} and perovskite, reaching a V_{OC} of 1.234 V. (**C**) Intensity-dependent open-circuit voltage V_{OC} with linear fits (dashed lines). (**D**) Pseudo–*J-V* curves reconstructed from intensity-dependent absolute PL measurements on the illustrated sample stack. The 2PACz and Me-4PACz curves almost coincide; the dashed lines represent pseudo–*J-V* curves from the sample variations including the electron-selective C_{60} layer, with which all curves are comparable because of the limiting nonradiative recombination at the C_{60} interface. (**E**) Pseudo–*J-V* curves reconstructed from the measurements in (C). Table 1 summarizes the FF values extracted from the pseudo–*J-V* curves. (**F**) Repartition of loss mechanisms lowering the cell's FF below the detailed balance limit, comparing PTAA and Me-4PACz cells: nonradiative loss in neat material (= radiative FF limit minus pFF of neat film), nonradiative interface loss (= pFF of neat film minus pFF of full cell), and transport loss (= pFF of full cell minus FF of measured solar cell).

Table 1. Comparison of "pseudo" fill factors (pFF) and implied open-circuit voltages (*i*V_{OC}). The values were derived from suns-PL and suns-V_{OC} measurements for our perovskite film on all studied hole-selective layers and on quartz glass. The table also shows the maximum FF attained in *J-V* measurements (max FF) (see also Fig. 3). "Half cell" refers to substrate/HTL/absorber, whereas "full cell" denotes the complete solar cell including C_{60}, SnO_2 and Ag metal electrode.

	Quartz glass	PTAA	MeO-2PACz	2PACz	Me-4PACz
pFF (%), half cell (suns-PL)	87.9	85.6	85.5	88.3	87.5
pFF (%), half cell + C_{60} (suns-PL)	85.3	85.3	85.3	85.3	85.3
pFF (%), full cell (suns-V_{oc})		85.8	85.9	86.9	87.9
max FF (%), full cell (*J-V*)		79.8	81.9	81.8	84.0
iV_{OC} (V), half cell (absolute PL)	1.258	1.185	1.215	1.244	1.248
n_{ID}, full cell (suns-V_{OC})		1.55	1.51	1.42	1.26

differences between the studied HTLs for the *i*V_{OC} and pFF were apparent (Fig. 3D, dashed lines; Table 1, row 2), as the C_{60} layer sets an *i*V_{OC} limitation through high nonradiative recombination rates (*53*). This limitation was only overcome with a counter electrode on the C_{60} (Fig. 3E and full devices), which underscores the role of the dipoles that Me-4PACz and 2PACz created at the ITO surface. The calculated molecular dipole value of the hole-transporting fragment is ~0.2 D for MeO-2PACz, ~1.7 D for Me-4PACz, and ~2 D for 2PACz. The positive dipoles shifted the work function of the ITO toward higher absolute numbers (fig. S2A), which presumably resulted in a higher built-in potential throughout the device (*55*, *56*). A well-defined built-in potential can exist with the presence of a second electrode countering the ITO—in this case, Ag or Cu. Thus, when reconstructing the *J-V*s from the suns-V_{OC} measurement on full devices in Fig. 3C to extract the pFF (Table 1, row 3), both 2PACz and Me-4PACz overcame the pFF and *i*V_{OC} limitations imposed by the C_{60} layer (Fig. 3E).

The differences between the electrical *J-V* curves (max. FF 84%) in Fig. 3B and pseudo–*J-V* curves (max. FF ~88%) arose from transport losses caused by the finite mobility of the C_{60}, non-optimized sample design, and ITO sheet resistance, as well as the measurement setup. Figure 3F summarizes a comparison of the different contributions to FF losses for PTAA

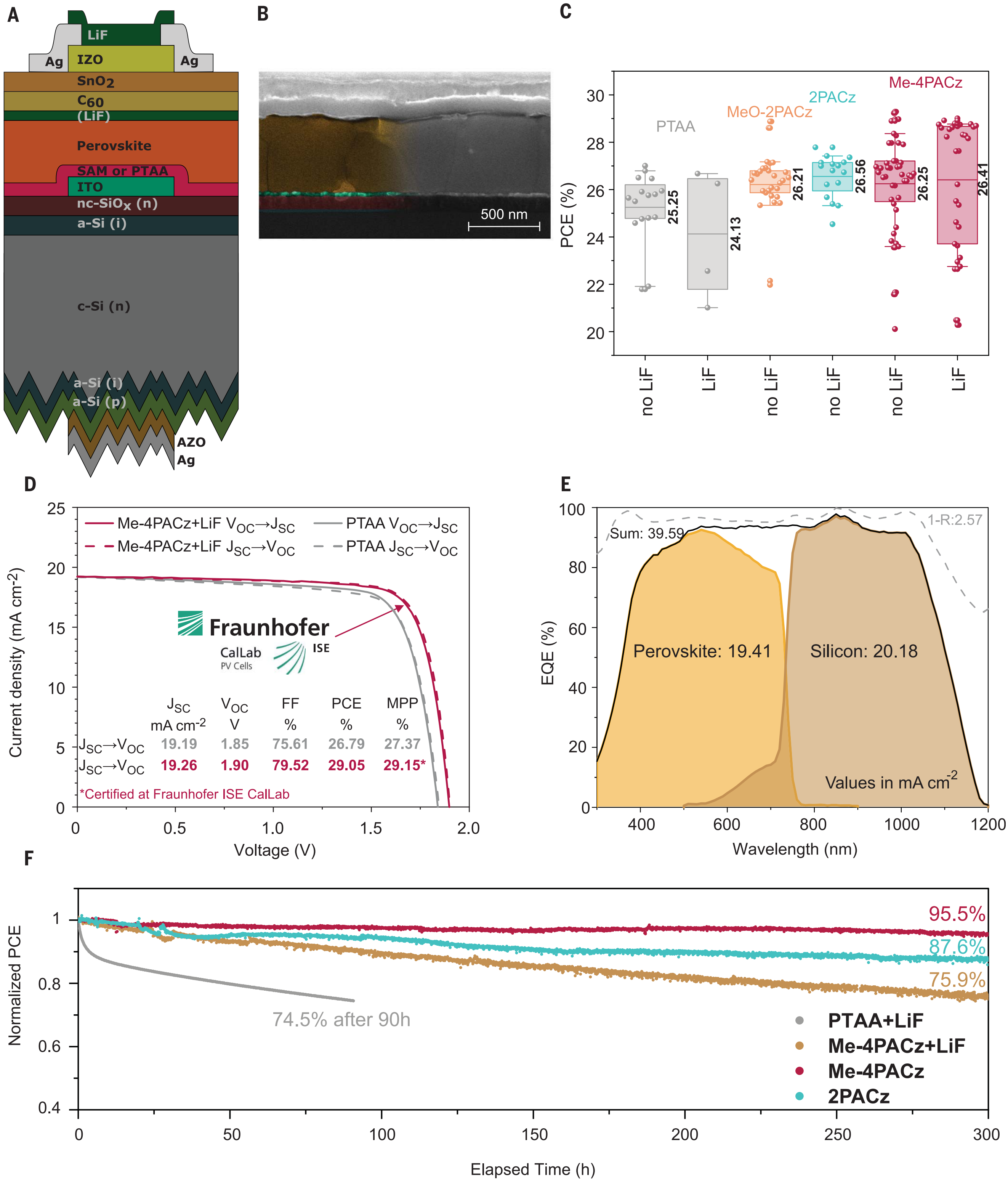

Fig. 4. Characteristics of monolithic perovskite/silicon tandem solar cells using various HTLs. (**A**) Schematic stack of the monolithic perovskite/silicon tandem solar cell. (**B**) SEM image of a tandem cross section with Me-4PACz as HTL. (**C**) Statistics of the PCE of PTAA, MeO-2PACz, 2PACz, and Me-4PACz tandem solar cells from *J-V* scans. (**D**) Certified *J-V* curve measured at Fraunhofer ISE, including the MPP value and the device parameters (red), in comparison to a tandem cell with PTAA (gray) as HTL measured in-house. (**E**) External quantum efficiency (EQE) and reflection (denoted as 1-R) of the certified tandem cell measured in-house. The AM1.5G-equivalent current densities are given. (**F**) Long-term MPP track using a dichromatic LED illumination of nonencapsulated solar cells in air at a controlled temperature of 25°C and relative humidity of 30 to 40%. The data are normalized to the MPP average of the first 60 min of each individual track to account for measurement noise. Because of the fast degradation, the MPP track of the PTAA + LiF cell is normalized to the first recorded value. The legend specifies each HTL and notes whether a LiF interlayer was used.

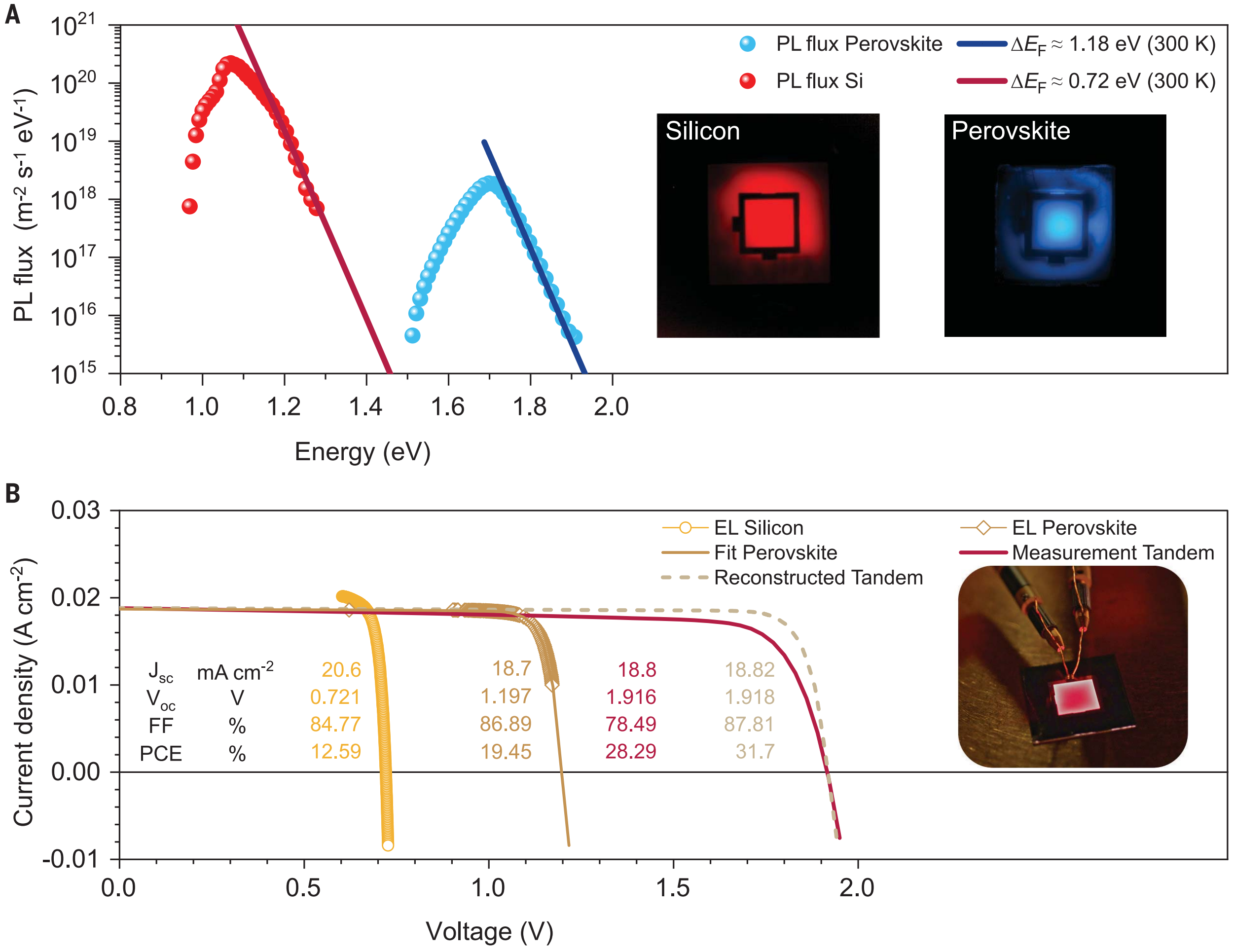

Fig. 5. Luminescence subcell analysis of a tandem solar cell with Me-4PACz and LiF interlayer. (**A**) Absolute PL spectra of the subcells recorded under 1-sun equivalent illumination. The excitation wavelengths are 455 nm and 850 nm for the perovskite and silicon subcell, respectively. PL images constructed from the integrated PL fluxes are also shown. The edge length of the active area (inner square) is 1 cm. (**B**) Reconstructed *J-V* curves calculated from injection-dependent electroluminescence (EL) measurements (open symbols) and shifted by the photogenerated current density. Furthermore, the perovskite subcell is fitted with a single-diode model (solid brown line). The reconstructed tandem *J-V* (dashed line) was calculated by adding the voltages of the subcells for each current density. The *J-V* measurement under simulated 1-sun illumination of this cell is shown as a solid red line. Furthermore, a photograph of the tandem solar cell at high injection current is shown. Due to a bandgap of 1.68 eV, the subcell emits light in the visible wavelength range and thus, the emission is visible by eye and with a regular digital camera.

and Me-4PACz, derived from comparisons of the pseudo–*J-V* curves to the measured *J-V* curves and radiative limits, as previously reported by Stolterfoht *et al.* (*54*). In addition to nonradiative losses at the PTAA interface (red), the film thickness (~10 nm, versus <1 nm with a SAM) and low conductivity of the PTAA led to greater transport losses than with Me-4PACz.

Integration into monolithic perovskite/silicon tandem solar cells

Efficient passivation in combination with fast hole extraction of Me-4PACz in perovskite single junctions could be transferred into monolithic tandem solar cells, which led to higher FF, V_{OC}, and stability. A schematic stack of this solar cell is shown in Fig. 4A. We used a silicon heterojunction solar cell as the bottom cell (*26*), based on a 260-µm-thick n-type float-zone Si wafer processed as described in the supplementary materials. The textured rear side enhanced the near-infrared (NIR) absorption, whereas the polished front side enabled the deposition of spin-coated perovskite. The 20-nm ITO recombination layer also served as the anchoring oxide for the SAMs (*7*). The top cell, with the same 1.68-eV perovskite bandgap and nominal precursor composition $Cs_{0.05}(FA_{0.77}MA_{0.23})_{0.95}Pb(I_{0.77}Br_{0.23})_3$ as analyzed above, formed the single-junction stack of ITO/HTL/perovskite/(LiF)/C_{60}/SnO_2/IZO/Ag/LiF. Figure 4B shows a scanning electron microscopy (SEM) cross-section image of a part of the tandem solar cell; no obvious differences were observed between perovskite films on the different HTLs (fig. S24). The molecular SAM cannot be resolved with SEM. Figure S25 shows a photograph and layout of the tandem device.

Figure 4C compares the PCE of tandem solar cells based on PTAA, MeO-2PACz, 2PACz, and Me-4PACz, with and without a LiF interlayer at the perovskite/C_{60} interface. With PTAA, the LiF interlayer led to rapid degradation of the cells (see fig. S26 for individual parameters). Without the interlayer, we achieved an average PCE of 25.25%. In contrast, the average efficiency of MeO-2PACz and 2PACz was 26.21% and 26.56%, respectively. The use of a LiF interlayer for Me-4PACz cells increased the V_{OC} but reduced the FF. Thus, both configurations reached a similar average PCE of 26.25% and 26.41%, respectively. However, with Me-4PACz the maximum PCEs (<29%) are higher than cells with 2PACz, mainly because of higher FF of up to 81%. These high FF values were achieved despite almost all cells being perovskite-limited (table S1). The statistics of all photovoltaic parameters are shown in fig. S26. The *J-V* measurements of the champion cells of each configuration are shown in fig. S28; the PV parameters are summarized in table S2.

The tandem solar cells did not reach FF values comparable to those in single-junction cells because of the larger active area (1 cm^2) and a transparent conductive oxide (TCO) without grid fingers, leading to increased series resistance. The cells showed very high V_{OC} values of up to 1.92 V (fig. S30). With a V_{OC} of ~715 mV from the bottom cell at half illumination (fig. S31), the contribution of the perovskite subcell was ~1.2 V. Figure 4D shows a direct comparison between champion PTAA and Me-4PACz tandem cells; besides the 50-mV improvement in V_{OC}, the enhanced hole extraction boosted the FF by ~4% absolute.

We sent a tandem cell with Me-4PACz and a LiF interlayer to Fraunhofer ISE CalLab for independent certification (Fig. 4D; see fig. S32 for certificate). With a V_{OC} of 1.90 V, FF of 79.4%, and a short-circuit current density J_{SC} of 19.23 mA cm^{-2}, the cell had a PCE of 29.01% when measuring from J_{SC} to V_{OC}, similar to our in-house measurement (fig. S33) and was certified at the MPP with a PCE of 29.15% with a designated area of 1.064 cm^2. This PCE surpasses other monolithic (*10*, *27*) and four-terminal perovskite-based tandem solar cells (*57*) and is on par with the best GaAs single cell with the same active area (*27*).

Figure 4E shows the external quantum efficiency (EQE) of the certified tandem cell. Under AM1.5G-equivalent illumination conditions, the photogenerated current densities J_{ph} in the perovskite and silicon subcells were 19.41 mA cm^{-2} and 20.18 mA cm^{-2}, respectively, which agreed with the measured J_{SC} of 19.23 mA cm^{-2}. The tandem solar cell exhibited a nonideal current mismatch of 0.77 mA cm^{-2}, and even though the perovskite cell sets the slope around 0 V, the cell reached a FF of 79.5%. The cumulative photogenerated current density and loss caused by reflection were 39.59 mA cm^{-2} and 2.57 mA cm^{-2}, respectively. A comparison of EQEs and reflection losses between a cell of this work (planar front side) and a fully textured cell by Sahli *et al.* (*58*) is shown in fig. S34.

After the certification, we fabricated more Me-4PACz tandem solar cells without a LiF interlayer (fig. S26), which showed average performance similar to that with LiF. The champion cell showed a higher FF of 81% and lower V_{OC} of 1.87 V than without LiF. Together with a J_{SC} of 19.37 mA cm^{-2}, this led to a PCE of 29.29% and a stabilized efficiency of 29.32% (fig. S35).

We measured the stability of different nonencapsulated tandem solar cells (Fig. 4F). To track the degradation induced by either the top or the bottom cell more carefully, we developed a dichromatic LED setup using LEDs with center emission wavelengths of 470 nm and 940 nm (fig. S36) and with independent intensity calibration and recording. We adjusted the mismatch so that the J_{ph} in the individual subcells was equal to that measured under AM1.5G-equivalent illumination to maintain proper stability tracking of monolithic tandem solar cells (see below and supplementary text). The devices were measured under continuous MPP load (using voltage perturbation), at 25°C and in ambient air with 30 to 40% relative humidity. The photogenerated current densities of the subcells are given in table S3 and set which subcell is limiting. The degradation for a perovskite-limited tandem cell with Me-4PACz+LiF showed 75.9% of its initial efficiency (29.13%) after 300 hours. When we substituted the Me-4PACz with PTAA (perovskite-limited), the PCE decreased to 74.5% of its initial PCE (25.9%) after only 90 hours.

We additionally tracked a cell with Me-4PACz as HTL without a LiF interlayer to test the intrinsic stability of the HTL/perovskite combination. After 300 hours, the cell still operated at 95.5% of its initial PCE. Although the cells were current-matched, this track monitors a degradation of the perovskite, as it directly translates into the performance of the tandem cell and no degradation of the Si subcell is expected within these time scales. Our comparison strongly suggests that the use of a LiF interlayer reduces the stability. As described in other reports (*59*–*62*), the decrease in stability might be caused by deterioration of the electrodes and C_{60} interface upon migration of Li^+ and F^- ions. We note that it is important to declare the mismatch conditions because the use of a NIR-poor spectrum would lead to a Si-limited cell and thus to a higher stability (see supplementary text). Comparing this result to state-of-the-art stability tests of nonencapsulated tandem solar cells in ambient conditions, where the cells retained 90% of initial PCE after 61 hours (*58*) and 92% after 100 hours (*13*), our Me-4PACz tandem solar cell showed a superior operational stability.

In addition to the long-term stability measurements at 25°C, we conducted an MPP track of a Me-4PACz tandem cell at elevated temperatures. Following the procedure of Jošt *et al.*, the temperature was successively increased from 25° to 85°C and back to 25°C (*63*). There was no loss in PCE after this 200-min procedure, despite the high MA and Br amount of the wide-bandgap perovskite used here (fig. S39).

Subcell *J-V* characteristics of a monolithic tandem solar cell

One downside of monolithic multijunction solar cells is that the subcell characteristics are barely accessible. External quantum efficiency measurements are the only subcell-resolved measurements presented in almost all publications reporting multijunction solar cells. Here, we used absolute PL measurements in each subcell of a representative tandem solar cell (Me-4PACz + LiF). With this, we could estimate the QFLS, and thus the V_{OC} was accessible for both subcells independently. For this, we used hyperspectral absolute PL imaging at equivalent 1-sun conditions with an illumination spot larger than the area of the solar cells. The PL spectra and the integrated images are shown in Fig. 5A.

From the high-energy slope of the absolute PL spectra of the subcells, the individual implied V_{OC} values were calculated: 1.18 V for the perovskite subcell and 0.72 V for the Si subcell (*18*, *64*). From the PL spectra, we calculated the PLQY of both subcells, yielding values of 1.5% for Si and 0.02% for the perovskite. PLQY values exceeding 5% have already been demonstrated in perovskite single-junction devices for lower bandgaps (*19*).

To estimate the pseudo–*J-V* curves of the subcells, we performed absolute EL imaging, where the excess charge carriers are generated electrically to access the subcell characteristics (*65*–*68*). For each injected current, an EL image was recorded, from which the voltage of the subcells can be calculated from an average over the active area (fig. S40). With the reconstructed pseudo–*J-V* curves from injection current–dependent EL imaging, we analyzed the maximum possible efficiency of this cell stack with minimized charge transport losses (see supplementary materials for more details). We reconstructed both subcell *J-V* curves by calculating the implied voltage at each injected current, yielding a "pseudo" light–*J-V* (JV_{EL}) curve for each subcell after shifting it by the respective photogenerated current density J_{ph} calculated from EQE measurements; these J_{ph} values amounted to 18.7 and 20.6 mA cm^{-2} for the top and bottom cell, respectively. The open symbols in Fig. 5B show the measured EL data points averaged over the perovskite and silicon subcell and shifted by their respective J_{ph} values.

For the perovskite, we additionally fitted the data with a single-diode model to display the *J-V* curve over the whole voltage range, which was otherwise not accessible during the EL measurement. To obtain the tandem JV_{EL}, we added the voltages of the subcells for each current density. The dashed line shows the result. The reconstructed curve deviated from the electrically measured *J-V* curve under a solar simulator. This is mainly because EL gave access only to the internal voltage, whereas an electrical *J-V* curve displays the current density versus external voltage (which is affected by series resistances; see supplementary text). Hence, a high FF (87.8%) of the JV_{EL} can be regarded as the maximum achievable value for this particular tandem cell if the electrodes and all charge-selective layers were free of series resistance losses. This would give a PCE of 31.7%, surpassing the theoretical PCE maximum of a silicon single cell (29.4%) (*69*). Thus, this cell stack has the capacity to overcome the 30% barrier through technical optimization of the contacts alone. However, by adjusting the mismatch conditions, even higher efficiencies are achievable.

To find the requirements for the highest efficiency, we fit the silicon subcell with a single-diode model. We conducted SPICE (Simulation Program with Integrated Circuit Emphasis) simulations to sweep the photogenerated current densities in the subcell. The single-diode models of the silicon and perovskite subcells were connected in series (schematically shown in fig. S42A), and the cumulative current density was fixed to 39.3 mA cm^{-2} (as calculated from EQE measurements for AM1.5G-equivalent illumination). Figure S42B shows the photovoltaic parameters as a function of the mismatch ($J_{ph,Si} - J_{ph,Pero}$). As shown in a previous publication, the V_{oc} is almost independent of the mismatch, whereas the FF is affected by it (*26*). A minimum FF occurs when the $J_{ph,Si}$ is 0.7 mA cm^{-2} below the $J_{ph,Pero}$. However, simultaneously the J_{SC} is highest under this condition. In a current-matching situation, the highest efficiency is 32.43%. This sets an estimation for the efficiency potential upon reduction of all transport losses. Decreasing the limitations set by the hole extraction speed, as shown in this work, is a viable path for exploring this potential.

REFERENCES AND NOTES

1. A. De Vos, *J. Phys. D* **13**, 839–846 (1980).
2. W. Shockley, H. J. Queisser, *J. Appl. Phys.* **32**, 510–519 (1961).
3. S. E. Sofia *et al.*, *Sustain. Energy Fuels* **4**, 852–862 (2020).
4. Z. Li *et al.*, *Joule* **2**, 1559–1572 (2018).
5. National Renewable Energy Laboratory, Best Research-Cell Efficiency Chart; www.nrel.gov/pv/cell-efficiency.html.
6. T. Todorov *et al.*, *Adv. Energy Mater.* **5**, 1500799 (2015).
7. A. Al-Ashouri *et al.*, *Energy Environ. Sci.* **12**, 3356–3369 (2019).
8. R. Lin *et al.*, *Nat. Energy* **4**, 864–873 (2019).
9. G. E. Eperon *et al.*, *Science* **354**, 861–865 (2016).
10. D. Kim *et al.*, *Science* **368**, 155–160 (2020).
11. J. Xu *et al.*, *Science* **367**, 1097–1104 (2020).
12. Y. Hou *et al.*, *Science* **367**, 1135–1140 (2020).
13. B. Chen *et al.*, *Joule* **4**, 850–864 (2020).
14. M. Jošt, L. Kegelmann, L. Korte, S. Albrecht, *Adv. Energy Mater.* **10**, 1904102 (2020).
15. Y. Jiang *et al.*, *J. Mater. Chem. C* **4**, 5679–5689 (2016).
16. I. L. Braly *et al.*, *Nat. Photonics* **12**, 355–361 (2018).
17. D. W. deQuilettes *et al.*, *ACS Energy Lett.* **1**, 438–444 (2016).
18. T. Kirchartz, J. A. Márquez, M. Stolterfoht, T. Unold, *Adv. Energy Mater.* **10**, 1904134 (2020).
19. Z. Liu *et al.*, *ACS Energy Lett.* **4**, 110–117 (2019).
20. P. Caprioglio *et al.*, *Sustain. Energy Fuels* **3**, 550–563 (2019).
21. Q. Jiang *et al.*, *Nat. Photonics* **13**, 460–466 (2019).
22. S. Yang *et al.*, *J. Am. Chem. Soc.* **141**, 5781–5787 (2019).
23. L. Krückemeier, U. Rau, M. Stolterfoht, T. Kirchartz, *Adv. Energy Mater.* **10**, 1902573 (2020).
24. P. K. Nayak, S. Mahesh, H. J. Snaith, D. Cahen, *Nat. Rev. Mater.* **4**, 269–285 (2019).
25. A. Rajagopal, R. J. Stoddard, S. B. Jo, H. W. Hillhouse, A. K. Y. Jen, *Nano Lett.* **18**, 3985–3993 (2018).
26. E. Köhnen *et al.*, *Sustain. Energy Fuels* **3**, 1995–2005 (2019).
27. M. A. Green *et al.*, *Prog. Photovolt. Res. Appl.* **28**, 3–15 (2020).
28. P. Caprioglio *et al.*, *Adv. Energy Mater.* **10**, 2000502 (2020).
29. M. A. Green, A. W. Y. Ho-Baillie, *ACS Energy Lett.* **4**, 1639–1644 (2019).
30. K. Jäger, L. Korte, B. Rech, S. Albrecht, *Opt. Express* **25**, A473–A482 (2017).
31. M. Jošt *et al.*, *Energy Environ. Sci.* **11**, 3511–3523 (2018).
32. T. Leijtens, K. A. Bush, R. Prasanna, M. D. McGehee, *Nat. Energy* **3**, 828–838 (2018).
33. E. T. Hoke *et al.*, *Chem. Sci.* **6**, 613–617 (2015).
34. D. J. Slotcavage, H. I. Karunadasa, M. D. McGehee, *ACS Energy Lett.* **1**, 1199–1205 (2016).
35. S. Mahesh *et al.*, *Energy Environ. Sci.* **13**, 258–267 (2020).
36. M. Saliba *et al.*, *Energy Environ. Sci.* **9**, 1989–1997 (2016).
37. M. Stolterfoht *et al.*, *Energy Environ. Sci.* **12**, 2778–2788 (2019).
38. D. Luo *et al.*, *Science* **360**, 1442–1446 (2018).
39. Q. Wang *et al.*, *Adv. Energy Mater.* **9**, 1900990 (2019).
40. C. Huang *et al.*, *J. Am. Chem. Soc.* **138**, 2528–2531 (2016).
41. A. Torres, L. G. C. Rego, *J. Phys. Chem. C* **118**, 26947–26954 (2014).
42. M. Saliba *et al.*, *Nat. Energy* **1**, 15017 (2016).
43. Y. Lin *et al.*, *Nat. Commun.* **9**, 4981 (2018).
44. B. Chen *et al.*, *Adv. Mater.* **31**, e1902413 (2019).
45. N. Phung *et al.*, *Adv. Energy Mater.* **10**, 1903735 (2020).
46. B. Krogmeier, F. Staub, D. Grabowski, U. Rau, T. Kirchartz, *Sustain. Energy Fuels* **2**, 1027–1034 (2018).
47. F. Staub *et al.*, *Phys. Rev. Appl.* **6**, 044017 (2016).
48. M. Krumrey, G. Ulm, *Nucl. Instrum. Methods Phys. Res. A* **467–468**, 1175–1178 (2001).
49. D. Skroblin *et al.*, *Rev. Sci. Instrum.* **91**, 023102 (2020).
50. K. A. Bush *et al.*, *Nat. Energy* **2**, 17009 (2017).
51. J.-F. Guillemoles, T. Kirchartz, D. Cahen, U. Rau, *Nat. Photonics* **13**, 501–505 (2019).
52. J. Seo *et al.*, *Energy Environ. Sci.* **7**, 2642–2646 (2014).
53. M. Stolterfoht *et al.*, *Nat. Energy* **3**, 847–854 (2018).
54. M. Stolterfoht *et al.*, *Adv. Mater.* **32**, 2000080 (2020).
55. N. Tessler, Y. Vaynzof, *ACS Energy Lett.* **5**, 1260–1270 (2020).
56. W. Wang *et al.*, *Adv. Funct. Mater.* **30**, 1909755 (2020).
57. B. Chen *et al.*, *Nat. Commun.* **11**, 1257 (2020).
58. F. Sahli *et al.*, *Nat. Mater.* **17**, 820–826 (2018).
59. R. Quintero-Bermudez, J. Kirman, D. Ma, E. H. Sargent, R. Quintero-Torres, *J. Phys. Chem. Lett.* **11**, 4213–4220 (2020).
60. Z. Li *et al.*, *Energy Environ. Sci.* **10**, 1234–1242 (2017).
61. S.-M. Bang *et al.*, *ACS Energy Lett.* **5**, 1198–1205 (2020).
62. S. N. Habisreutinger *et al.*, *Nano Lett.* **14**, 5561–5568 (2014).
63. M. Jošt *et al.*, *Adv. Energy Mater.* **10**, 2000454 (2020).
64. T. Unold, L. Gütay, in *Advanced Characterization Techniques for Thin Film Solar Cells*, D. Abou-Ras, T. Kirchartz, U. Rau, Eds. (Wiley-VCH, 2011), pp. 151–175.
65. S. Chen *et al.*, *Sci. Rep.* **5**, 7836 (2015).
66. D. Alonso-Alvarez, N. Ekins-Daukes, *IEEE J. Photovoltaics* **6**, 1004–1011 (2016).
67. S. Roensch, R. Hoheisel, F. Dimroth, A. W. Bett, *Appl. Phys. Lett.* **98**, 251113 (2011).
68. D. Hinken, K. Ramspeck, K. Bothe, B. Fischer, R. Brendel, *Appl. Phys. Lett.* **91**, 182104 (2007).
69. A. Richter, M. Hermle, S. W. Glunz, *IEEE J. Photovoltaics* **3**, 1184–1191 (2013).

ACKNOWLEDGMENTS

We thank M. Gabernig, C. Ferber, T. Lußky, H. Heinz, C. Klimm, and M. Muske at the Institute for Silicon Photovoltaics, Helmholtz-Zentrum Berlin (HZB), and T. Hänel, T. Henschel, M. Zelt, H. Rhein, K. Meyer-Stillrich, and M. Hartig at PVcomB (HZB) for technical assistance. A.A.-A. thanks A. Merdasa for his expertise during construction of the steady-state PL setup. Ei.K. and S.A. thank C. Wolff (University of Potsdam) and K. Brinkmann (University of Wuppertal) for fruitful discussion at the beginning of the project. A.M. acknowledges A. Drevilkauskaite for help with the synthesis of 4PACz and 6PACz materials. **Funding:** Supported by Federal Ministry for Education and Research (BMBF) grant 03SF0540 within the project "Materialforschung für die Energiewende"; the Federal Ministry for Economic Affairs and Energy (BMWi)–funded project ProTandem (0324288C); the HyPerCells graduate school; the Helmholtz Association within the HySPRINT Innovation lab project and TAPAS project; the Helmholtz Association via HI-SCORE (Helmholtz International Research School) (M.G., P.C., S.A., and D.N.); the European Union's Horizon 2020 research and innovation program under grant agreement 763977 of the PerTPV project; the Research Council of Lithuania under grant agreement S-MIP-19-5/SV3-1079 of the SAM project (A.M. and T.M.); Slovene Research Agency (ARRS) funding through research programs P2-0197 and J2-1727 (M.J., G.M., and M.T.); Deutsche Forschungsgemeinschaft projects 423749265 and 03EE1017C-SPP 2196 (SURPRISE and HIPSTER) (M.S., D.N., and S.A.); EPSRC and D. Lidzey for Ph.D. studentship funding via CDT-PV (EP/L01551X/1) (J.A.S.); and Erasmus+ (J.A.S.). **Author contributions:** A.A.-A., Ei.K., B.L., and S.A. planned the experiments, coordinated the work,and prepared the figures; Er.K., A.M., and T.M. designed and synthesized the Me-4PACz SAM and the (Me-)nPACz series; A.A.-A. and B.L. processed the single-junction cells and optimized the SAM deposition; Ei.K. and B.L. processed the tandem cells; A.B.M.V. processed the Si bottom cells; A.A.-A., H.H., and J.A.M. conducted and analyzed the PL experiments; J.A.M., A.A.-A., and Ei.K. performed the EL studies. H.H. recorded the terahertz measurements and performed the data analysis; P.C., M.G., and M.S. conducted the pseudo–*J-V* and FF-V_{OC} loss analysis (intensity-dependent V_{OC} and QFLS); D.M. performed the photoelectron spectroscopy; J.A.S., D.S., and N.P. performed crystallographic analysis; G.M., M.J., B.L., and Ei.K. designed and built the tandem aging setup and recorded the long-term MPP tracks; and S.A., V.G., M.S., T.U., T.M., C.G., R.S., M.T., La.K., A.A., D.N., B.S., and B.R. supervised the projects. All authors contributed to data interpretation and manuscript writing. **Competing interests:** HZB and Kaunas University of Technology have filed patents for the SAM molecules described above and their use in tandem solar cells. **Data and materials availability:** All data are available in the main text or the supplementary materials.

SUPPLEMENTARY MATERIALS

science.sciencemag.org/content/370/6522/1300/suppl/DC1
Materials and Methods
Supplementary Text
Figs. S1 to S39
Tables S1 to S3
References (*70*–*85*)

19 June 2020; accepted 30 October 2020
10.1126/science.abd4016

Science

Monolithic perovskite/silicon tandem solar cell with >29% efficiency by enhanced hole extraction

Amran Al-Ashouri, Eike Köhnen, Bor Li, Artiom Magomedov, Hannes Hempel, Pietro Caprioglio, José A. Márquez, Anna Belen Morales Vilches, Ernestas Kasparavicius, Joel A. Smith, Nga Phung, Dorothee Menzel, Max Grischek, Lukas Kegelmann, Dieter Skroblin, Christian Gollwitzer, Tadas Malinauskas, Marko Jost, Gasper Matic, Bernd Rech, Rutger Schlatmann, Marko Topic, Lars Korte, Antonio Abate, Bernd Stannowski, Dieter Neher, Martin Stolterfoht, Thomas Unold, Vytautas Getautis and Steve Albrecht

Science **370** (6522), 1300-1309.
DOI: 10.1126/science.abd4016

Efficiency from hole-selective contacts

Perovskite/silicon tandem solar cells must stabilize a perovskite material with a wide bandgap and also maintain efficient charge carrier transport. Al-Ashouri *et al.* stabilized a perovskite with a 1.68–electron volt bandgap with a self-assembled monolayer that acted as an efficient hole-selective contact that minimizes nonradiative carrier recombination. In air without encapsulation, a tandem silicon cell retained 95% of its initial power conversion efficiency of 29% after 300 hours of operation.

Science, this issue p. 1300

ARTICLE TOOLS	http://science.sciencemag.org/content/370/6522/1300
SUPPLEMENTARY MATERIALS	http://science.sciencemag.org/content/suppl/2020/12/09/370.6522.1300.DC1
REFERENCES	This article cites 83 articles, 6 of which you can access for free http://science.sciencemag.org/content/370/6522/1300#BIBL
PERMISSIONS	http://www.sciencemag.org/help/reprints-and-permissions

Science (print ISSN 0036-8075; online ISSN 1095-9203) is published by the American Association for the Advancement of Science, 1200 New York Avenue NW, Washington, DC 20005. The title *Science* is a registered trademark of AAAS.